# Elastic moduli of untreated, demineralized and deproteinized cortical bone: Validation of a theoretical model of bone as an interpenetrating composite material

E. Hamed [a], E. Novitskaya [b], J. Li [a], P.-Y. Chen [b,c], I. Jasiuk [a,*], J. McKittrick [b]

[a] University of Illinois at Urbana – Champaign, Department of Mechanical Science and Engineering, 1206 West Green Street, Urbana, IL 61801, USA
[b] University of California, San Diego, Department of Mechanical and Aerospace Engineering and Materials Science and Engineering Program, 9500 Gilman Dr., La Jolla, CA 92093, USA
[c] National Tsing Hua University, Department of Materials Science and Engineering, 101 Sec. 2 Kuang-Fu Rd., Hsinchu 30013, Taiwan, ROC

## ARTICLE INFO

## ABSTRACT

A theoretical experimentally based multi-scale model of the elastic response of cortical bone is presented. It portrays the hierarchical structure of bone as a composite with interpenetrating biopolymers (collagen and non-collagenous proteins) and minerals (hydroxyapatite), together with void spaces (porosity). The model involves a bottom-up approach and employs micromechanics and classical lamination theories of composite materials. Experiments on cortical bone samples from bovine femur include completely demineralized and deproteinized bones as well as untreated bone samples. Porosity and microstructure are characterized using optical and scanning electron microscopy, and micro-computed tomography. Compression testing is used to measure longitudinal and transverse elastic moduli of all three bone types. The characterization of structure and properties of these three bone states provides a deeper understanding of the contributions of the individual components of bone to its elastic response and allows fine tuning of modeling assumptions. Very good agreement is found between theoretical modeling and compression testing results, confirming the validity of the interpretation of bone as an interpenetrating composite material.

## 1. Introduction

Bone tissue is a natural composite material consisting of an organic phase (90% type-I collagen and 10% non-collagenous proteins (NCP)), an inorganic phase (hydroxyapatite-like minerals) and water. On a volumetric basis, mammalian skeletal bone is made up of 32–44% organics, 33–43% minerals and 15–25% water [1]. These constituents assemble into a complex hierarchical structure, which gives bone its excellent mechanical properties [2–4]. In this paper, the hierarchical structure of cortical bone is described in terms of four structural levels (Fig. 1), spanning from nanoscale to mesoscale levels.

Nanoscale (Level I), which ranges from a few to several hundred nanometers, represents a mineralized collagen fibril level. A mineralized fibril has a composite structure made of organic and inorganic phases and water. Type I collagen, which is the major constituent of the organic phase, consists of triple helical tropocollagen molecules which are ~300 nm long [5,6] and ~1.5 nm in diameter [6,7]. These molecules assemble into a staggered arrangement with a periodicity of 67 nm [8,9], which includes gap and overlap regions. The inorganic phase consists of non-stoichiometric hydroxyapatite crystals ($Ca_{10}(PO_4)_6(OH)_2$), with 4–6% of the phosphate groups replaced by carbonate groups. The mineral crystals are in the form of platelets 40–60 nm long, 20–30 nm wide and 2–4 nm thick [10–14]. The remaining phase is water, which plays an important role in bio-mineralization. These constituents are combined into mineralized collagen fibrils (~100–200 nm in diameter [1,15]), which are the primary building blocks of bone. It is generally believed that crystals initially form within the gap regions of the collagen fibrils, further proceed into the overlap regions, and subsequently grow into the extrafibrillar space [16,17]. Consequently, minerals are found both within and outside the collagen fibrils, but the exact amount in each location is still a matter of contention [18–22]. Recent studies [23–25] on completely deproteinized and completely demineralized bones show that both the minerals and protein form continuous phases.

Sub-microscale (Level II), which spans from one to tens of microns, represents a single lamella level. A lamella, with thickness 3–7 μm [10], is made of preferentially oriented mineralized collagen fibrils. At this length scale, the elliptical cavities called lacunae (typically 5–10 μm wide and 15–25 μm long [26,27]) can be observed. Connecting the lacuna are small channels (~100–500 nm in diameter [28]), called canaliculi.

Microscale (Level III), ranging from tens to hundreds of microns, denotes lamellar structures, which are made of lamellae stacked together at different orientations, i.e., the fibrils in each lamella are oriented at a different angle with respect to the adjacent one
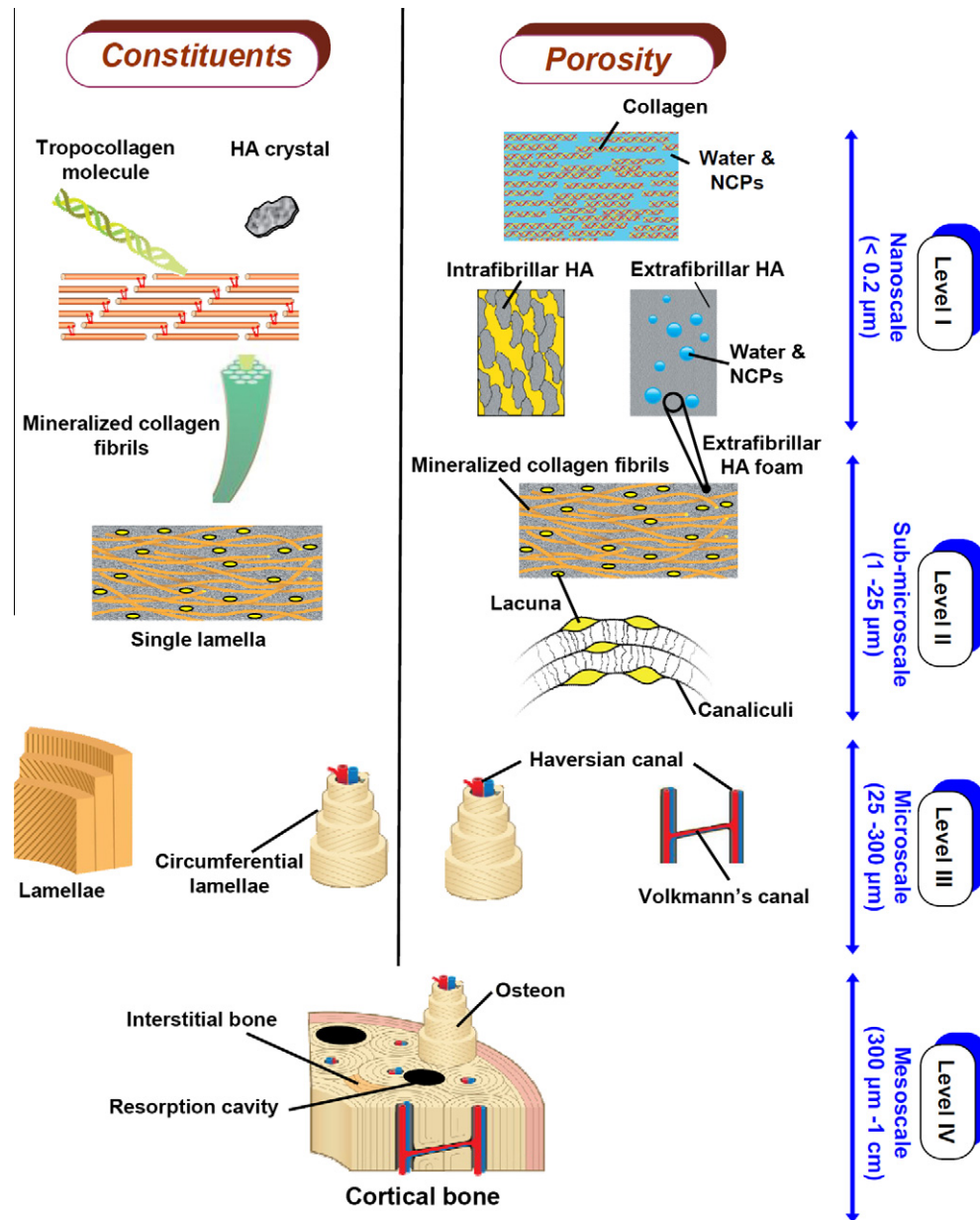
**Fig. 1.** Hierarchical structure of cortical bone constituents and associated porosity. HA = hydroxyapatite, NCP = non-collagenous proteins.

| | Constituents | Porosity |
|---|---|---|
| I | At the nanoscale, tropocollagen molecules ($\sim300 \times 1.5 \times 1.5$ nm) and hydroxyapatite minerals ($50 \times 25 \times 3$ nm) combine to form the basic unit of all bone—the mineralized collagen fibril ($\sim100$ nm in diameter). | Gaps within and between the collagen molecules ($\sim40–100$ nm) configure the first level of porosity, where minerals, water, and non-collagenous proteins are deposited. |
| II | Lamellae (3–7 µm thick) are formed from preferentially oriented mineralized collagen fibrils. | Embedded in the lamellae are lacuna spaces ($\sim25 \times 10 \times 5$ µm) where bone cells reside, connected by small channels (canaliculi). |
| III | The lamellae form osteons with a central vascular channel (Haversian system, 100–200 µm diameter), the primary feature of cortical bone. The orientation of the mineralized collagen fibrils is different between the adjacent lamellae, which form a twisted plywood structure. | Porosity at this level includes the Haversian canals ($\sim50$ µm in diameter), which are oriented longitudinally, and Volkmann's canals ($\sim50$ µm in diameter), which are oriented in transverse direction. |
| IV | Osteonal and interstitial bones with resorption cavities form the cortical bone. | Resorption cavities ($\sim300$ µm in diameter), sites of bone remodeling, are the main porosity at this scale. |

[29,30]. In cortical bone, several layers of the lamellae, arranged in concentric rings around the vascular channels, form osteons (Haversian system), while interstitial lamellae, which are remnants of old osteons, fill spaces between osteons.

Mesoscale (Level IV), which spans several hundred microns to several millimeters or more, depending on species, represents the cortical bone level. The cortical bone consists of osteons embedded in interstitial lamellae with some resorption cavities.

In order to understand the structure and mechanical properties of bone and its protein and mineral constituents, bone can be demineralized or deproteinized by aging in HCl or NaOCl solutions, respectively. Previous studies on the structure of cancellous and

cortical bones [23–25] showed that, after complete deproteinization and demineralization, the bone samples maintained structural integrity, and the mineral and protein constituents showed surprisingly similar microstructures and retained features such as Haversian systems, lacunae and canaliculi. Compression tests on untreated (UT), demineralized (DM) and deproteinized (DP) cancellous [31] and cortical bones [25] showed that the mechanical properties of DM and DP bone are much lower than those of UT bone. These results indicate that bone is an interpenetrating composite material whose properties are enhanced by the intertwining of the two phases: proteins and minerals.

The structure of bone is more complex than that of most engineering composite materials and modeling of its mechanical properties has long been a challenging task. In the literature, a number of theoretical studies have addressed the mechanical properties of UT bone at different hierarchical levels. At the nanoscale, most of the existing models consider bone as a composite material made up of collagen matrix and hydroxyapatite inclusions [32,33] or, conversely, hydroxyapatite matrix and collagen inclusions [34,35]. There are also a few models representing collagen and crystals as two interpenetrating phases [34,36]. Computational models, involving a finite element method, have also been used to investigate the collagen–mineral interactions in bone [37–40]. However, in such models the hydroxyapatite phase is treated as disconnected crystals rather than a continuous phase. At the submicrostructural level, Jasiuk and Ostoja-Starzewski [41] modeled a single lamella as a spatially random network of mineralized collagen fibrils and computed its effective anisotropic stiffness tensor. Fritsch and Hellmich [36] and Yoon and Cowin [42] used micromechanics methods to obtain the effective elastic properties of a single lamella. At the microstructural level, Dong and Guo [43] modeled a single osteon as a two-phase composite with osteonal lamellae being a matrix and a Haversian canal being an inclusion in the form of an elongated pore. They also extended their micromechanical model to assess the elastic properties of cortical bone by modeling the interstitial lamellae as a matrix, and osteons and resorption cavities as inclusions [43]. There are also other models that capture the elastic behavior of UT cortical bone. However, there are no multi-scale models of DM and DP cortical bones available in the literature.

In this study, the elastic moduli of the UT, DM and DP cortical bone are investigated. A step-by-step modeling approach, involving four different hierarchical levels (Levels I–IV), is proposed, and theoretical results at the cortical bone level (mesoscale) are compared with compression test data. The experimental observations on the structure and composition of these three bone types serve as inputs for the theoretical model. To the authors' knowledge, this is the first report on the development of the multi-scale model that incorporates experimental observations of bone as an interpenetrating composite material composed of contiguous biopolymer and mineral phases.

## 2. Materials and experimental methods

### 2.1. Sample preparation

A single fresh bovine femur bone from an animal of unknown breed was obtained from a local butcher (La Jolla, CA). The slaughter age was ~18 months. Samples, ~3 cm thick, were cut from the mid-diaphysis region. The bone was thoroughly cleaned with water, and soft tissue was removed with a scalpel. Sixty cortical bone samples ($5 \times 5 \times 7.5$ mm) were prepared for compression testing of UT, DM and DP bones (20 samples for each bone type). The samples were first roughly cut with a handsaw and then precisely with a diamond blade under constant water irrigation,

with the compression surfaces cut as parallel as possible. An aspect ratio of 1.5 was chosen in order to reduce the influence of sample surface traction forces, according to Ref. [44], which suggested using an aspect ratio between one and two for compression samples. Samples were prepared for testing in two directions: longitudinal and transverse. The longitudinal direction was chosen along the long axis of the bone, while the transverse direction was perpendicular to the long axis in the circumferential (angular) direction. Ten samples of each bone type were prepared for each testing direction. Samples were wrapped in a wet paper towel, placed in plastic zipped bags and stored in a refrigerator ($T = 4 \,^\circ\text{C}$) for 1–2 days until chemical treatment and mechanical testing. The paper towels were moistened with Hank's balanced saline solution (HBSS). HBSS was chosen because it is a standard saline solution recommended for storage and hydration of bone and other mineralized tissues [45].

### 2.2. Demineralization and deproteinization process

Cortical bone samples were demineralized by aging in 0.6 N hydrochloric acid (HCl) at room temperature, following the procedures described in Refs. [24,46]. Acid solutions were changed daily in order to avoid saturation, which can affect the demineralization process. The complete demineralization process took ~7 days. All solutions were quantitatively analyzed by inductively coupled plasma optical emission spectrometry, to evaluate the Ca concentration. The completeness of demineralization was verified by the absence of Ca in the solutions. Bone samples were deproteinized by aging in a 5.6 wt.% sodium hypochloride (NaOCl) solution at 37 °C, following the procedures in Ref. [24]. The solutions were changed every 12 h. The whole process took about 2 weeks. Full deproteinization was verified by subsequent demineralization, which resulted in the disappearance of the sample (deproteinization followed by demineralization). Previous work on bone demineralization and deproteinization showed that the amount of proteins left in the solution after subsequent demineralization of previously DP samples is <0.001 wt.% [24].

### 2.3. Structural characterization

In order to estimate the area fractions of osteonal and interstitial lamellae, ten representative images of five different UT bone samples, all obtained from the same femur, were used for analysis by optical microscopy (OM) using a Zeiss Axio imager equipped with a CCD camera (Zeiss Microimaging Inc., Thornwood, NY). Optical images were taken at $100\times$ and $200\times$ in order to view significant bone features clearly.

Fracture surfaces of the specimens from all three groups were analyzed by scanning electron microscopy (SEM) equipped with energy dispersive spectroscopy (FEI-XL30, FEI Company, Hillsboro, OR). DM bone samples were subjected to critical point drying procedure with a purge time equal to 20 min. using the fully automatic critical point drier (Tousimis Autosamdri-815, Rockville, MD) before SEM imaging in order to avoid excessive shrinkage and deformation. Samples from all groups were mounted on aluminum sample holders, air dried and sputter-coated (Emitech K575X, Quorum Technologies Ltd., West Sussex, UK) with chromium for 30 s before imaging. Samples were observed at a 20 kV accelerating voltage with a working distance of 10 mm.

OM and SEM images gave two-dimensional (2-D) information about bone microstructure. To investigate the microstructure in three-dimensions (3-D), the micro-computed tomography (μ-CT) imaging was performed on the three bone groups at a nominal isotropic resolution of 1 μm. This allowed for high-resolution 3-D imaging without destruction of the specimen. The scan produced ~1024 slices ($1024 \times 1024$ image pixels per slice) resulting in a

field of view (FOV) of roughly 1 mm³ cube. The μ-CT measurements were conducted in air using Xradia MicroXCT-200 (for UT and DP samples) and MicroXCT-400 (for DM samples) (Xradia Inc., Pleasanton, CA) instruments. The two instruments were chosen based on the range of X-ray electric potential they could acquire. Samples were scanned at various X-ray photon energies, depending on their physical properties, to obtain optimum imaging. Scanning of the DM group was performed at low energies (30 kV, 200 μA; acquirable only on MicroXCT-400) owing to low X-ray absorption of proteins, while the DP group required high energies (80 kV, 100 μA). For UT samples, the parameter was set between the two treated cases (40 kV, 200 μA). For all measurements 729 projections were acquired over a range of 182° with 12 s exposure time for each projection. No frame averaging was taken at each tomography projection. The data were reconstructed using Xradia TXMReconstructor. Ring artifacts and beam hardening effects (BHE) were corrected in the reconstruction software. For the DP group (hydroxyapatite only), the BHE were pronounced and, therefore, a beam-flattening filter was placed in the X-ray path during the scan.

The reconstructed μ-CT tomograms were post-processed using Amira (Visage Imaging, Inc., Berlin, Germany) to analyze 3-D microstructures. No filtering was applied on images of UT samples, while for treated cases (DM and DP) the median filter was applied to suppress noises and enhance image contrast. The gray image slices were then segmented to binarized data sets, separating voids from bone regions. The threshold value was critically judged around the middle point between two peaks corresponding to bone and voids in the gray level histogram [47]. After image segmentation, the 3-D microstructures were reconstructed, and quantitative analysis was implemented to obtain the 3-D morphometric information.

### 2.4. Compression testing

Specimens from the three groups (UT, DM and DP) were submerged in HBSS for 24 h before testing and were tested in the hydrated condition (the time between taking the samples out from the solution and testing them was ∼1 min). Novitskaya et al. [25] showed that the saline solution fills all pores generated by removal of protein or mineral phases, which significantly affects the corresponding mechanical properties. Compression testing was performed with a 30 kN load cell universal testing machine (Instron 3367 Dual Column Testing System, Norwood, MA) on UT samples, while a 500 N load cell testing machine (Instron 3342 Single Column Testing System) was used on DM and DP samples. Specimens were tested at a 0.5 mm min⁻¹ crosshead speed, which translated to a strain rate of $10^{-3}$ s⁻¹. An external deflectometer SATEC model I3540 (Epsilon Technology Corp., Jackson, WY) was used to measure small displacements with a precision linearity reading of 0.25% of full measuring range. Compression tests were performed in the unconstrained conditions.

## 3. Modeling methods

In this section, the multi-scale approach for modeling of cortical bone is introduced which consists of successive homogenization steps from nano to mesoscale levels (Levels I–IV). The effective elastic properties of UT, DM and DP cortical bones at each structural level were found in a "bottom-up" fashion, using the results from a lower level as the inputs for a higher level. Continuum micromechanics methods and classical lamination theory of composite materials were employed to account for the microstructure of bone at different scales. The elastic properties and volume fractions of the constituents (collagen, hydroxyapatite, water and NCP) were the main inputs to the model. A wide range of values for the elastic moduli of collagen and hydroxyapatite has been reported in the literature (see Table 1 in Ref. [48]). The choice of properties for bone constituents is tabulated in Table 1. For simplicity, in the present model, all components were assumed to be linear elastic and isotropic. The model is well suited to account for anisotropy. However, there are limited data in the literature on a complete set of anisotropic constants for collagen and hydroxyapatite crystals. Table 2 lists definitions of all the symbols and abbreviations used throughout the modeling sections.

### 3.1. Modeling of UT cortical bone

#### 3.1.1. Nanoscale—Level I

At the nanoscale, water and NCP fill the spaces between collagen and hydroxyapatite, and solid phases interact with water [42]. Therefore, the properties of collagen should be considered in its wet state. Following Ref. [36], a Mori–Tanaka scheme [49,50], with the cross-linked collagen molecules being a matrix and the intermolecular voids (filled with water and NCP) being the inclusions, was used to obtain the effective elastic properties of collagen–water composite $\mathbf{C}_{colw}$ as

$$\mathbf{C}_{colw} = \mathbf{C}_{col} + \Phi_w \left\{ (\mathbf{C}_w - \mathbf{C}_{col}) : \left[ \mathbf{I} + \mathbf{S}_{col}^{sph} : \mathbf{C}_{col}^{-1} : (\mathbf{C}_w - \mathbf{C}_{col}) \right]^{-1} \right\}$$
$$: \left\{ \Phi_{col} \mathbf{I} + \Phi_w \left[ \mathbf{I} + \mathbf{S}_{col}^{sph} : \mathbf{C}_{col}^{-1} : (\mathbf{C}_w - \mathbf{C}_{col}) \right]^{-1} \right\}^{-1}, \quad (1)$$

where subscripts "colw", "col" and "w" refer, respectively, to collagen–water composite, dry collagen, and water and NCP. The derivation of elastic stiffness tensors of collagen $\mathbf{C}_{col}$ and water with NCP $\mathbf{C}_w$ is given in Appendix A. $\mathbf{S}_0^r$ is the fourth-order Eshelby tensor [51] accounting for the shape of phase $r$ in a matrix with stiffness tensor $\mathbf{C}_0$, where 0 is a generic subscript. Here, superscript "sph" denotes the shape of spherical void inclusions.

Moreover, mineral crystals have some internal defects (porosities). Thus, a mineral interacting with water can be represented as a porous solid with some intercrystalline voids within, filled with water and NCP. The Mori–Tanaka method was applied to predict the stiffness of hydroxyapatite–water mixture $\mathbf{C}_{HAw}$, as follows

$$\mathbf{C}_{HAw} = \mathbf{C}_{HA} + \Phi_w \left\{ (\mathbf{C}_w - \mathbf{C}_{HA}) : \left[ \mathbf{I} + \mathbf{S}_{HA}^{sph} : \mathbf{C}_{HA}^{-1} : (\mathbf{C}_w - \mathbf{C}_{HA}) \right]^{-1} \right\}$$
$$: \left\{ \Phi_{HA} \mathbf{I} + \Phi_w \left[ \mathbf{I} + \mathbf{S}_{HA}^{sph} : \mathbf{C}_{HA}^{-1} : (\mathbf{C}_w - \mathbf{C}_{HA}) \right]^{-1} \right\}^{-1}. \quad (2)$$

In Eq. (2), subscripts "HAw" and "HA" denote, respectively, hydroxyapatite–water composite and hydroxyapatite crystals. The elastic stiffness of hydroxyapatite $\mathbf{C}_{HA}$ is given by Eq. (A.1) in Appendix A.

A mineralized collagen fibril was modeled as a nanocomposite material using a micromechanics continuum approach involving a self-consistent method [52,53] with two interpenetrating phases: collagen–water mixture and interfibrillar hydroxyapatite–water composite. The self-consistent formulation developed for polycrystalline materials was used such that there was no distinct matrix, and both phases were represented as ellipsoidal inclusions. The collagen–water phase was assumed to be cylindrical in shape with an aspect ratio of 1000:1:1 following the ∼100 μm length [54] and ∼100 nm diameter of collagen fibrils [1,15], while hydroxyapatite–water minerals were represented as ellipsoids with an aspect ratio of 50:25:3 following Ref. [55]. The effective stiffness tensor of a mineralized collagen fibril $\mathbf{C}_{fib}$, given in terms of stiffness tensors of collagen–water $\mathbf{C}_{colw}$ and interfibrillar hydroxyapatite–water $\mathbf{C}_{HAw}$, was predicted as

**Table 1**
Elastic properties and volume fractions of bone constituents employed in the modeling.

| Material | Young's modulus (GPa) | Poisson's ratio | Volume fraction (%) |
|---|---|---|---|
| Collagen | 1.5 [32,84] | 0.28 [20] | 41 |
| Hydroxyapatite | 114 [85,86] | 0.23 [87] | 42 |
| Non-collagenous proteins | 1.0 [20] | 0.45 [20] | 4 |
| | Bulk modulus (GPa) | Poisson's ratio | Volume fraction (%) |
| Water | 2.3 | 0.49 | 13 |

**Table 2**
Symbols used in the modeling and their definitions.

| Symbol | Definition |
|---|---|
| $\mathbf{C}$ | Elastic stiffness tensor |
| $cfib$ | Hydroxyapatite coated fibril |
| $col$ | Dry collagen |
| $colw$ | Collagen–water composite |
| $cyl$ | Cylinder |
| DOM | Degree of mineralization |
| $Efoam$ | Extrafibrillar hydroxyapatite foam |
| $ellipse$ | Ellipse |
| $fib$ | Mineralized collagen fibril |
| HA | Hydroxyapatite crystal |
| HAw | Hydroxyapatite–water composite |
| $\mathbf{I}$ | Identity tensor |
| $llam$ | Interstitial lamellae |
| $lac$ | Lacuna |
| NCP | Non-collagenous protein |
| $os$ | Osteon |
| $p$ | Pores (due to resorption cavities) |
| $\Phi$ | Volume fraction |
| $\mathbf{S}$ | Eshelby tensor |
| $sph$ | Sphere |
| $w$ | Water and non-collagenous proteins |

$$\mathbf{C}_{fib} = \left\{ \Phi_{colw}\mathbf{C}_{colw} : \left[\mathbf{I} + \mathbf{S}_{fib}^{cyl} : \mathbf{C}_{fib}^{-1} : (\mathbf{C}_{colw} - \mathbf{C}_{fib})\right]^{-1} \right.$$
$$\left. + \Phi_{HAw}\mathbf{C}_{HAw} : \left[\mathbf{I} + \mathbf{S}_{fib}^{ellipse} : \mathbf{C}_{fib}^{-1} : (\mathbf{C}_{HAw} - \mathbf{C}_{fib})\right]^{-1} \right\}$$
$$: \left\{ \Phi_{colw}\left[\mathbf{I} + \mathbf{S}_{fib}^{cyl} : \mathbf{C}_{fib}^{-1} : (\mathbf{C}_{colw} - \mathbf{C}_{fib})\right]^{-1} \right.$$
$$\left. + \Phi_{HAw}\left[\mathbf{I} + \mathbf{S}_{fib}^{ellipse} : \mathbf{C}_{fib}^{-1} : (\mathbf{C}_{HAw} - \mathbf{C}_{fib})\right]^{-1} \right\}^{-1}, \quad (3)$$

where subscript "$fib$" denotes the mineralized collagen fibril. Here, superscripts "$cyl$" and "$ellipse$" refer, respectively, to the cylindrical and ellipsoidal shapes of collagen and hydroxyapatite. Since the effective properties of a mineralized collagen fibril $\mathbf{C}_{fib}$ were not isotropic, the components of the Eshelby tensor were evaluated numerically for an ellipsoidal inclusion embedded in a general anisotropic matrix [56]. Eq. (3) was solved iteratively, with Eshelby tensors $\mathbf{S}_{fib}^{cyl}$ and $\mathbf{S}_{fib}^{ellipse}$ being updated at each iteration, to obtain the implicit unknown $\mathbf{C}_{fib}$. The elastic constants of a mineralized collagen fibril $\mathbf{C}_{fib}$ obtained in this level were then used as inputs for the next level.

### 3.1.2. Sub-microscale—Level II

At the sub-microstructural level, two different modeling steps were defined as in Ref. [48]: (1) mineralized collagen fibrils interacting with an extrafibrillar hydroxyapatite foam (coated fibrils), and (2) combining the matrix of step 1 with lacunar cavities to form a single lamella.

Different experimental techniques confirmed the existence of extrafibrillar hydroxyapatite crystals on the outer surface of the fibrils [19,22,57,58]. These crystals are dispersed and randomly oriented [59–61]. Therefore, the extrafibrillar hydroxyapatites can be treated as a porous foam consisting of hydroxyapatite minerals with intercrystalline pores in-between, filled with water and NCP [34,36,62,63]. The self-consistent scheme with two interpenetrating phases, hydroxyapatite–water minerals and pores, was used to evaluate the overall elastic constants of the extrafibrillar foam $\mathbf{C}_{Efoam}$ as

$$\mathbf{C}_{Efoam} = \left\{ \Phi_w\mathbf{C}_w : \left[\mathbf{I} + \mathbf{S}_{Efoam}^{sph} : \mathbf{C}_{Efoam}^{-1} : (\mathbf{C}_w - \mathbf{C}_{Efoam})\right]^{-1} \right.$$
$$\left. + \Phi_{HAw}\mathbf{C}_{HAw} : \left[\mathbf{I} + \mathbf{S}_{Efoam}^{sph} : \mathbf{C}_{Efoam}^{-1} : (\mathbf{C}_{HAw} - \mathbf{C}_{Efoam})\right]^{-1} \right\}$$
$$: \left\{ \Phi_w\left[\mathbf{I} + \mathbf{S}_{Efoam}^{sph} : \mathbf{C}_{Efoam}^{-1} : (\mathbf{C}_w - \mathbf{C}_{Efoam})\right]^{-1} \right.$$
$$\left. + \Phi_{HAw}\left[\mathbf{I} + \mathbf{S}_{Efoam}^{sph} : \mathbf{C}_{Efoam}^{-1} : (\mathbf{C}_{HAw} - \mathbf{C}_{Efoam})\right]^{-1} \right\}^{-1}, \quad (4)$$

where the subscript "$Efoam$" refers to the extrafibrillar hydroxyapatite foam. The random arrangement of extrafibrillar hydroxyapatite minerals leads to isotropy of the homogenized material. Therefore, for the sake of simplicity, both phases were assumed to be spherical in shape, following Ref. [64]. Furthermore, it was assumed that 75% of the total hydroxyapatite crystals were interfibrillar, and the remaining 25% were extrafibrillar [48].

Mineralized collagen fibrils, with the elastic properties obtained in Eq. (3), and the extrafibrillar hydroxyapatite foam, with the elastic properties obtained in Eq. (4), interpenetrate each other to form coated fibrils. The effective stiffness tensor of coated fibrils $\mathbf{C}_{cfib}$ was predicted by using the self-consistent scheme as

$$\mathbf{C}_{cfib} = \left\{ \Phi_{fib}\mathbf{C}_{fib} : \left[\mathbf{I} + \mathbf{S}_{cfib}^{cyl} : \mathbf{C}_{cfib}^{-1} : (\mathbf{C}_{fib} - \mathbf{C}_{cfib})\right]^{-1} + \Phi_{Efoam}\mathbf{C}_{Efoam} \right.$$
$$: \left[\mathbf{I} + \mathbf{S}_{cfib}^{sph} : \mathbf{C}_{cfib}^{-1} : (\mathbf{C}_{Efoam} - \mathbf{C}_{cfib})\right]^{-1} \right\}$$
$$: \left\{ \Phi_{fib}\left[\mathbf{I} + \mathbf{S}_{cfib}^{cyl} : \mathbf{C}_{cfib}^{-1} : (\mathbf{C}_{fib} - \mathbf{C}_{cfib})\right]^{-1} \right.$$
$$\left. + \Phi_{Efoam}\left[\mathbf{I} + \mathbf{S}_{cfib}^{sph} : \mathbf{C}_{cfib}^{-1} : (\mathbf{C}_{Efoam} - \mathbf{C}_{cfib})\right]^{-1} \right\}^{-1}. \quad (5)$$

In Eq. (5), subscript "$cfib$" refers to the mineralized collagen fibrils coated with extrafibrillar hydroxyapatite foam (coated fibrils). Also, superscripts "$cyl$" and "$sph$" denote, respectively, the cylindrical and spherical shapes of fibrils and extrafibrillar hydroxyapatite foam. Here again, two interpenetrating phases were considered, which were modeled as two different types of inclusions, with no matrix.

A single lamella was modeled as having coated fibrils as a matrix, with properties given in Eq. (5), perforated by osteocyte-filled ellipsoidal cavities called lacunae. Subscript "$lac$" denotes the ellipsoidal lacunae, with an aspect ratio of 5:2:1 following their approximate $25 \times 10 \times 5\ \mu m^3$ dimensions [26,42]. The major axes of lacunae were assumed to be oriented along the longitudinal direction of a single lamella. The effective elastic constants of a single lamella $\mathbf{C}_{lamella}$ were obtained using the Mori–Tanaka scheme as

$$\mathbf{C}_{lamella} = \mathbf{C}_{cfib} + \Phi_{lac}\left\{ (\mathbf{C}_{lac} - \mathbf{C}_{cfib}) : \left[\mathbf{I} + \mathbf{S}_{cfib}^{ellipse} : \mathbf{C}_{cfib}^{-1} : (\mathbf{C}_{lac} - \mathbf{C}_{cfib})\right]^{-1} \right\}$$
$$: \left\{ \Phi_{cfib}\mathbf{I} + \Phi_{lac}\left[\mathbf{I} + \mathbf{S}_{cfib}^{ellipse} : \mathbf{C}_{cfib}^{-1} : (\mathbf{C}_{lac} - \mathbf{C}_{cfib})\right]^{-1} \right\}^{-1}. \quad (6)$$

**Table 3**
3-D bone morphometry results from μ-CT image analysis.

| Porosity | | | Canals (UT samples only) | | Lacunae (UT samples only) | | |
|---|---|---|---|---|---|---|---|
| UT sample (%) | DM sample (%) | DP sample (%) | Volume fraction (%) | Mean width (μm) | Volume fraction (%) | Mean length (μm) | Mean width (μm) |
| 7.9 ± 0.81 | 51.5 ± 3.8 | 57.1 ± 3.5 | 4.4 ± 0.15 | 54.2 ± 4.8 | 3.6 ± 0.68 | 16.6 ± 2.8 | 7.0 ± 0.3 |
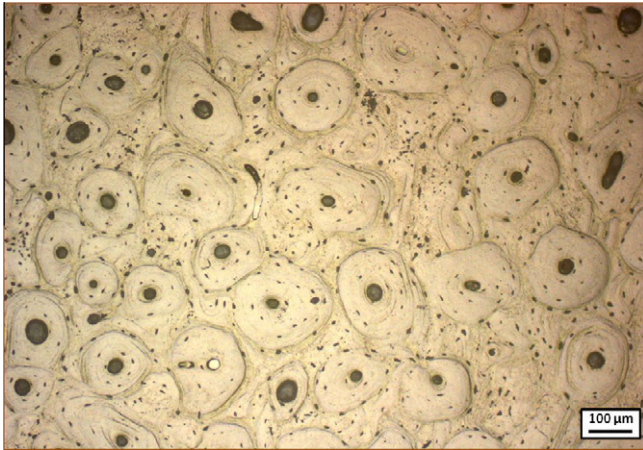


**Fig. 2.** Optical microscopy image of a cross section of bovine femoral cortical bone.

In the present model, the effect of canaliculi on elastic properties of the single lamella was neglected. The elastic properties of a single lamella $C_{lamella}$ were used as inputs for the next level.

### 3.1.3. Microscale—Level III

At the microscale, the lamellae are oriented in a twisted pattern characterized by a continuous rotation of lamellae. The properties of lamellae were obtained using Eq. (6), and the starting angle was chosen to be 0 degree for the innermost layer. To the authors' knowledge, there is no consensus in the literature on the number of lamellar layers in an osteon or the orientation of the outermost layer. Here, it was assumed that the fibrils complete a 180° turn from the innermost to the outermost layer. As long as the layers are not orthogonal to each other, the angle change between successive layers has a negligible effect on the results [65]. The elastic properties of an osteonal lamella were obtained following the homogenization scheme of Sun and Li [66] developed for laminated composite materials. More details on the modeling procedure of an osteonal lamella are given in Ref. [48].

The properties of an interstitial lamella were evaluated following the same homogenization procedure as for the osteonal lamella. The osteons are generally less stiff and less mineralized than the interstitial lamellae [67,68]. In order to capture such behavior, one could use a higher degree of mineralization (DOM) for an interstitial lamella compared with an osteonal lamella [48]. However, for simplicity here, both the osteonal and interstitial lamellae were assumed to have the same DOM and, therefore, the same elastic properties.

Having found the elastic properties of an osteonal lamella, a generalized self-consistent method [69] was used to calculate the effective elastic constants of an osteon $C_{os}$, following the approach of Dong and Guo [43]. To this end, the osteon was modeled as a two-phase composite with the osteonal lamella being a matrix and the Haversian canal being a cylindrical inclusion. An osteon
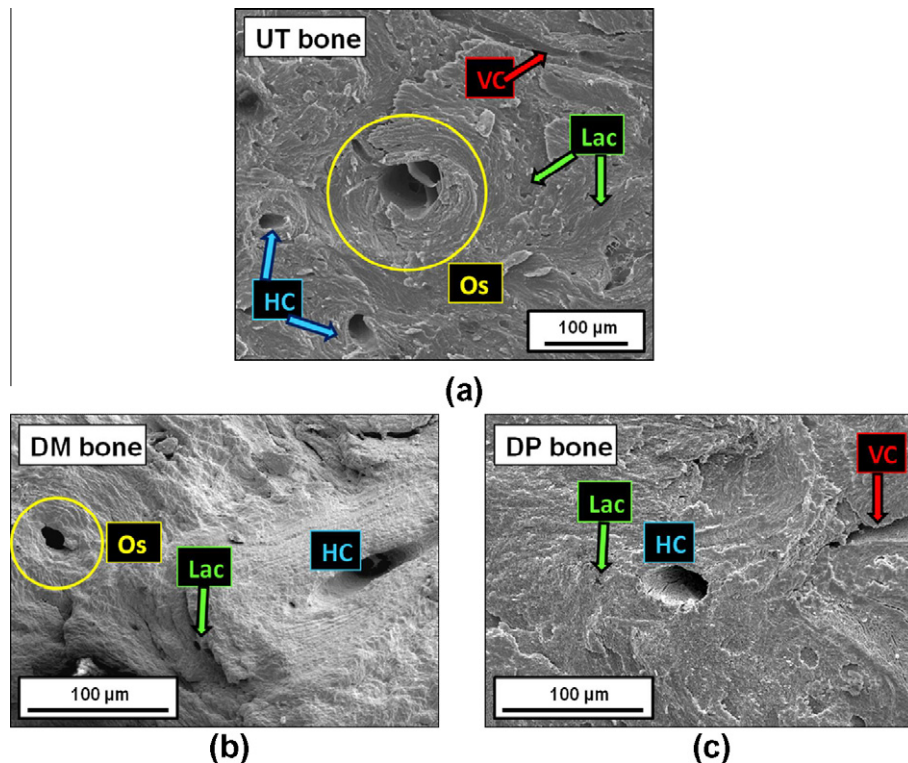


**Fig. 3.** SEM images of (a) untreated (UT), (b) demineralized (DM) (continuous protein network) and (c) deproteinized (DP) (continuous mineral network) cortical bones showing microstructural features: osteons (Os), lacuna spaces (Lac), Haversian channels (HC) and Volkmann's canals (VC).
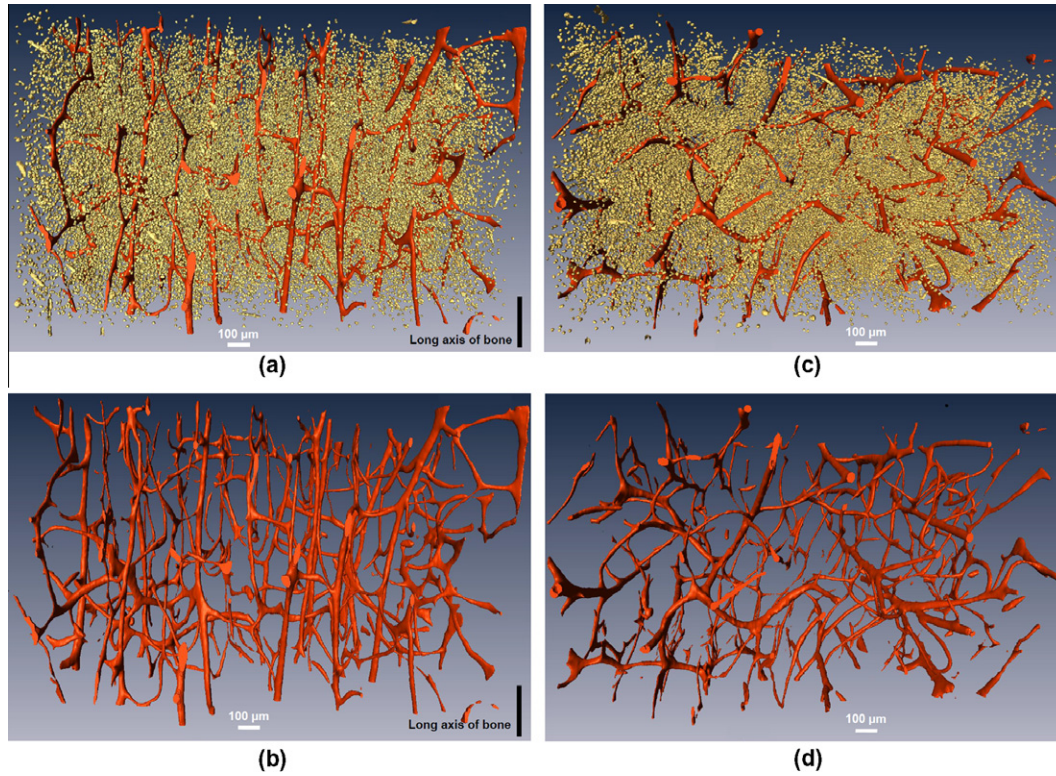
**Fig. 4.** μ-CT 3-D isosurface images of untreated (UT) cortical bone showing (a) side view of canal network (red: Haversian, vertical; Volkmann's, horizontal) and osteocyte lacunae (yellow); the lacunae are preferentially oriented in vertical direction, indicating the long axis of bone. (b) Side view of canal network only. (c) Top view of canal network and osteocyte lacunae. (d) Top view of canal network only. A volumetric filter ($20 \times 20 \times 20$ μm$^3$) was applied to separate the canal network from the lacuna space.

is typically a cylinder ~250 μm in diameter and ~1 cm long, while the diameter of the Haversian canal is ~50 μm [70]. Consequently, the volume fraction of the Haversian canals is ~4%. This choice for the volume fraction of longitudinal Haversian canals was also in good agreement with the present μ-CT findings (Table 3). The outputs of this level, which were the elastic stiffness tensors of an osteon $\mathbf{C}_{os}$ and an interstitial lamella $\mathbf{C}_{llam}$, served as the inputs for the next level.

### 3.1.4. Mesoscale—Level IV

The hybrid Mori–Tanaka scheme [71], with the interstitial lamella being the matrix and the osteons and resorption cavities being inclusions, was applied to evaluate the elastic constants of cortical bone at the mesoscale (tissue level). Both the osteons and the resorption sites were assumed to be cylindrical, with aspect ratios of 4:1:1, following the 1 cm length and 250 μm diameter of osteons [70], and aligned along the long axis of bone. The subscripts "llam", "os" and "p" denote the interstitial lamellae, osteons and pores, respectively. Then, the transversely isotropic effective stiffness tensor of the cortical bone $\mathbf{C}_{bone}$ was computed as

$$
\mathbf{C}_{bone} = \left\{ \Phi_{llam}\mathbf{C}_{llam} + \Phi_{os}\mathbf{C}_{os} : \left[\mathbf{I} + \mathbf{S}_{llam}^{cyl} : \mathbf{C}_{llam}^{-1} : (\mathbf{C}_{os} - \mathbf{C}_{llam})\right]^{-1} \right.
$$
$$
\left. + \Phi_p\mathbf{C}_p : \left[\mathbf{I} + \mathbf{S}_{llam}^{cyl} : \mathbf{C}_{llam}^{-1} : (\mathbf{C}_p - \mathbf{C}_{llam})\right]^{-1} \right\}
$$
$$
: \left\{ \Phi_{llam} + \Phi_{os}\left[\mathbf{I} + \mathbf{S}_{llam}^{cyl} : \mathbf{C}_{llam}^{-1} : (\mathbf{C}_{os} - \mathbf{C}_{llam})\right]^{-1} \right.
$$
$$
\left. + \Phi_p\left[\mathbf{I} + \mathbf{S}_{llam}^{cyl} : \mathbf{C}_{llam}^{-1} : (\mathbf{C}_p - \mathbf{C}_{llam})\right]^{-1} \right\}^{-1}. \tag{7}
$$

The volume fraction of osteons was taken as 68% based on the present optical images.

### 3.2. Modeling of treated cortical bone

Modeling of treated (DP and DM) bones followed the same modeling procedure as for the UT cortical bone with the following exceptions.

(i) In the treated bones, one phase was removed: the collagen in the case of DP bone, and the hydroxyapatite in the case of DM bone. The removed phase was replaced with voids in all the modeling steps. (ii) In the modeling of UT bone, it was assumed that half the volume fraction of water at nanoscale interacted with collagen, while the other half interacted with hydroxyapatite. However, in the case of treated bones, where one phase is no longer available, all the water content at nanoscale went to the remaining phase. In other words, in the case of DP bone, $\Phi_w = 0$ in Eq. (1), meaning that $\mathbf{C}_{colw} = \mathbf{C}_{col} \rightarrow \mathbf{0}$, whereas in the case of DM bone, $\Phi_w = 0$ in Eqs. (2) and (4), meaning that $\mathbf{C}_{HAw} = \mathbf{C}_{Efoam} = \mathbf{C}_{HA} \rightarrow \mathbf{0}$.

## 4. Results and discussion

Estimation of the amount of osteonal and interstitial bone area fractions was done by analyzing ten representative optical images of five different UT bone samples, all taken from the same femur (Fig. 2 is a representative optical image). The osteonal area fraction was found to be 0.68 ± 0.05, with the balance being the interstitial bone fraction; both area fractions incorporate their respective porosities. These numbers were later used in the present model for Level IV (mesoscale) as volume fractions.

SEM images of UT, DM and DP samples are shown in Fig. 3. Fig. 3a illustrates the fracture surface of an UT bone sample; vascular channels are visible and osteon structure is well defined. Fig. 3b and c demonstrate that DM and DP bones are contiguous, standalone structures (continuous protein network and continuous mineral network). Microscopic features, such as the Haversian
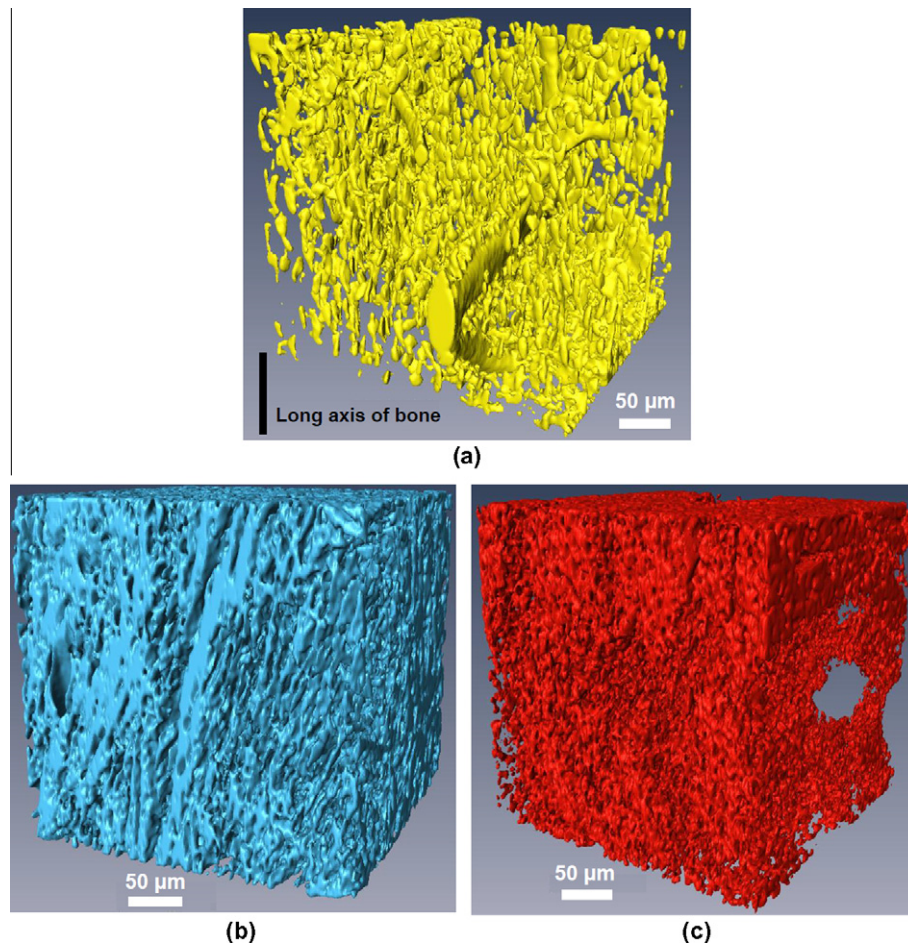
**Fig. 5.** μ-CT 3-D detailed surface view images of: (a) voids in untreated (UT) bone; the lacunae are preferentially oriented along the long axis of bone; (b) protein phase in demineralized (DM) bone; (c) mineral phase in deproteinized (DP) bone.

channels (20–40 μm in diameter) and Volkmann's canals, are preserved in DM and DP samples in agreement with Ref. [24]. Moreover, a well-defined osteon structure is clearly seen in both types of treated bone.

Fig. 4 shows the 3-D isosurface overview of all voids in the UT sample. The two types of porosity in sub-microscale to microscale levels, the osteocyte lacunar system and canal network, are clearly observed. The quantification was then performed on four samples per each group, and the results are presented in Table 3, which lists means and standard deviations. To illustrate 3-D microstructures in detail, a partial region inside ($300 \times 300 \times 300 \ \mu m^3$ cube) was chosen, and a complicated surface view was generated therein (Fig. 5). In UT bones, the lacunae have ellipsoid shapes that are oriented in the longitudinal direction of the bone. The collagen–fibril (Fig. 5b) and mineral-grain (Fig. 5c) like patterns are well observed in DM and DP bones, respectively.

Fig. 6 shows experimental stress–strain curves for UT, DM and DP cortical bones measured in longitudinal and transverse directions. UT and DP samples showed a well-defined initial linear elastic region, while DM samples showed the behavior typical for biopolymers with long "toe in" region in the initial part of the stress–strain curve. For UT bone, the longitudinal direction (with elastic modulus 22.76 ± 1.79 GPa) was stiffer and stronger than the transverse direction (with elastic modulus of 16.20 ± 1.44 GPa), in good agreement with the results of other researchers [3]. Removal of the mineral or protein phase resulted in a drastic change in the stress–strain curves. First, for the DM samples (Fig. 6b), the elastic modulus was calculated using the

steepest portions of the curves, and the modulus in the longitudinal direction (0.23 ± 0.01 GPa) was found to be larger than in the transverse direction (0.13 ± 0.02 GPa). As pointed out by Gibson and Ashby [72], the elastic modulus of a polymer foam is highly dependent on the density, and large deformations can be accommodated. The difference between the behavior in the longitudinal and transverse directions can be explained by the preferential orientation of the osteons, among other factors (see Refs. [73,74]). Secondly, the DP samples (Fig. 6c) appear to behave as a classic cellular solid, demonstrating a linear elastic region up to a peak stress, after which a plateau region is sustained. The longitudinal elastic modulus (9.23 ± 2.82 GPa) is larger than the transverse one (2.45 ± 0.78 GPa). This again can be attributed to the alignment of osteons in the longitudinal direction. As a side note, it is clear that a rule of mixtures law (Voigt average) does not apply here: the volume fraction averaged elastic modulus of the mineral and protein constituents (∼4.6 GPa in longitudinal direction) is not close to that of the UT bone.

Fig. 7a illustrates the modeling results for the longitudinal and transverse elastic moduli of UT cortical bone as a function of bone porosity. The same parameters are shown in Fig. 7b and c for DP and DM cortical bones, respectively. The range of porosities selected in the modeling for each bone type was based on the μ-CT measurements as listed in Table 3 (5–10% for UT bone, and 45–60% for DP and DM bones). Clearly, the elastic moduli of all three bone groups decrease as the porosity increases. Such a trend was also reported by other researchers for UT cortical bone [75,76] and for cellular structures [72,77], such as DP and DM bones.
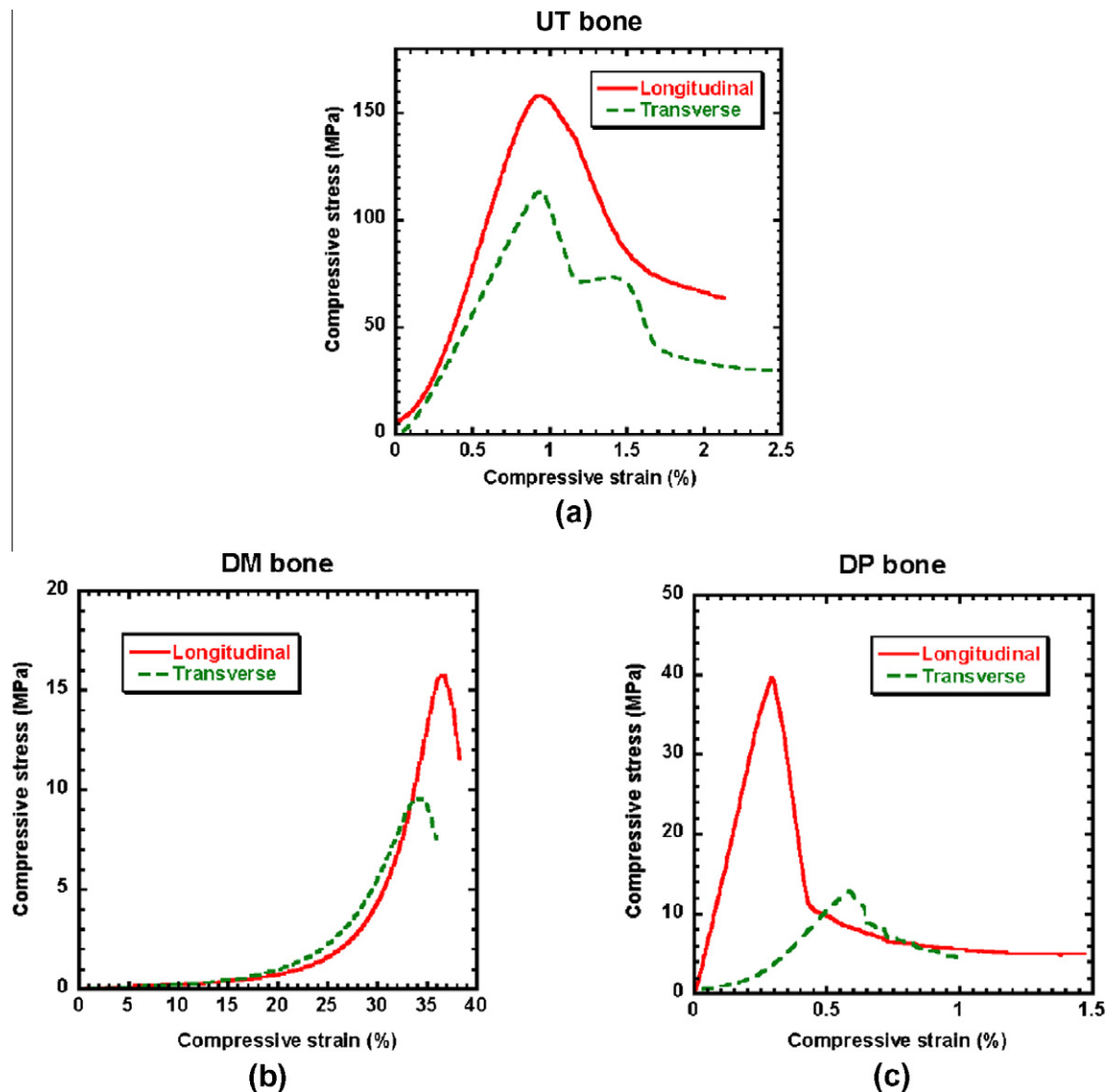
**Fig. 6.** Stress–strain curves for (a) untreated (UT), (b) demineralized (DM) and (c) deproteinized (DP) cortical bone for two anatomical directions. $N = 10$ for each curve.

Fig. 8 illustrates the experimental results obtained from compression testing for the longitudinal and transverse (in the circumferential direction) elastic moduli of UT, DP and DM cortical bones and compares them with modeling results. The mean values reported for theoretical results (Fig. 8) were calculated by averaging over the different values of porosity (Fig. 7). The bars in Fig. 8 represent the standard deviation and the range, respectively, for the experimental and modeling data. Experimental and modeling results are in very good agreement and, in most cases, their discrepancies, whenever present, are mainly due to simplifying assumptions and selections made at different stages of modeling. The main discrepancy between experiments and modeling occurs for the transverse elastic modulus of UT cortical bone. One possible reason may be that, in the present model, for simplicity, all osteons were assumed to be aligned along the long axis of bone. However, there are some drifting osteons in bone with off-axis, rather than the longitudinal, alignment [78]. The transverse elastic modulus of UT bone is underestimated by neglecting the presence of those misaligned osteons in the model. In addition, as mentioned in Section 3.1.3, in the present model the osteonal and interstitial lamellae were assumed to have the same DOM (42% mineral volume fraction [79]). The modeling results reported in Figs. 7 and 8 are based on that assumption. In reality, however, this is not the case,

and the interstitial lamellae are more mineralized than the osteonal lamellae. The present model can easily handle different mineral contents for interstitial and osteonal lamellae. In order to address this issue, first, the average mineral volume fraction was assumed to be 37% for osteon and 43% for interstitial lamella, following Gupta et al. [80], and the modeling steps were repeated for UT bone. In this case, the longitudinal and transverse elastic moduli were found to be, respectively, 19.63 and 8.91 GPa. Clearly, the values were lower compared with the previous results, since the overall mineral content became lower. Next, the case of 42% mineral volume fraction for osteons and 48% mineral volume fraction for interstitial bone was considered. The longitudinal elastic modulus of UT bone increased to 24.42 GPa, while the transverse modulus increased to 11.65 GPa. However, no experimental references support inputs of such higher mineral content. Ideally, the actual mineral content specific to the present bone type should be used in the model, but such measurements are not available for the present samples.

The other somewhat large discrepancy occurs between the theoretical and experimental longitudinal elastic modulus of DM bone. This can be explained by the fact that only the presence of longitudinal Haversian vascular channels was incorporated in the present model, but the existence of Volkmann's canals, which are
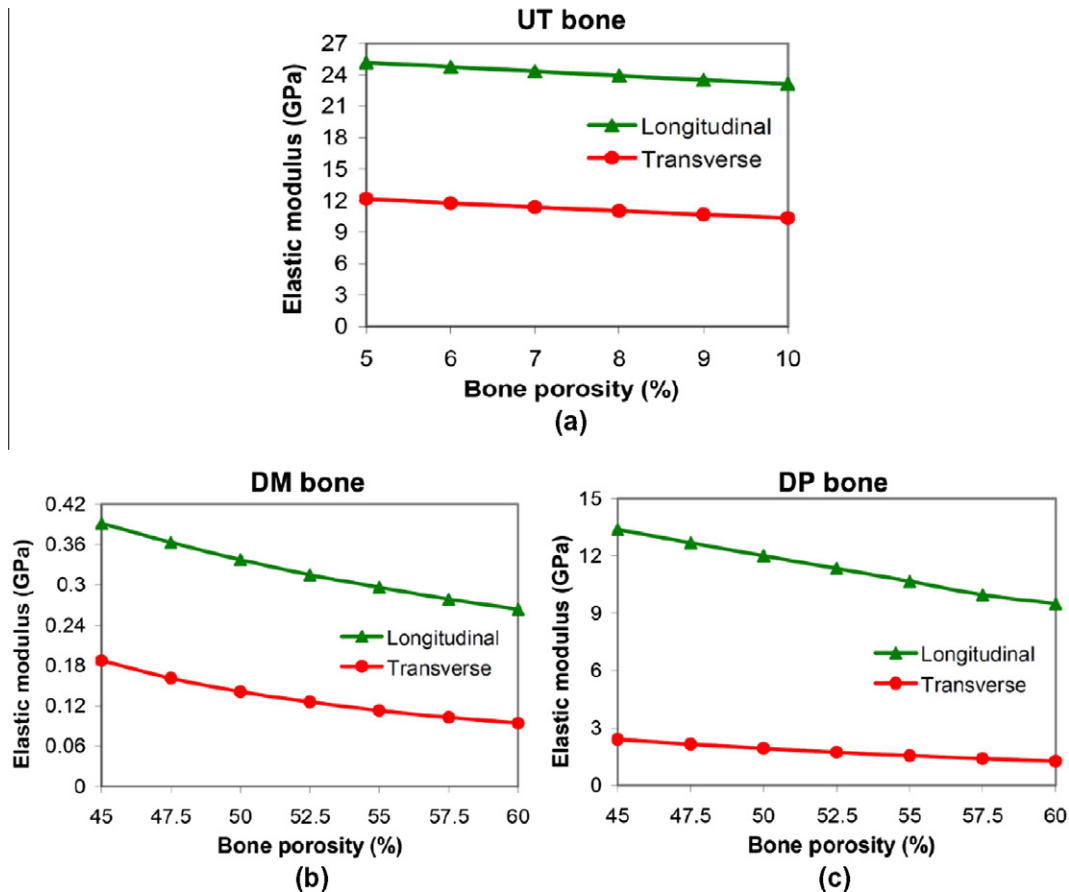
**Fig. 7.** Theoretical prediction of the elastic modulus as a function of porosity for longitudinal and transverse directions of (a) untreated (UT), (b) demineralized (DM) and (c) deproteinized (DP) cortical bone.
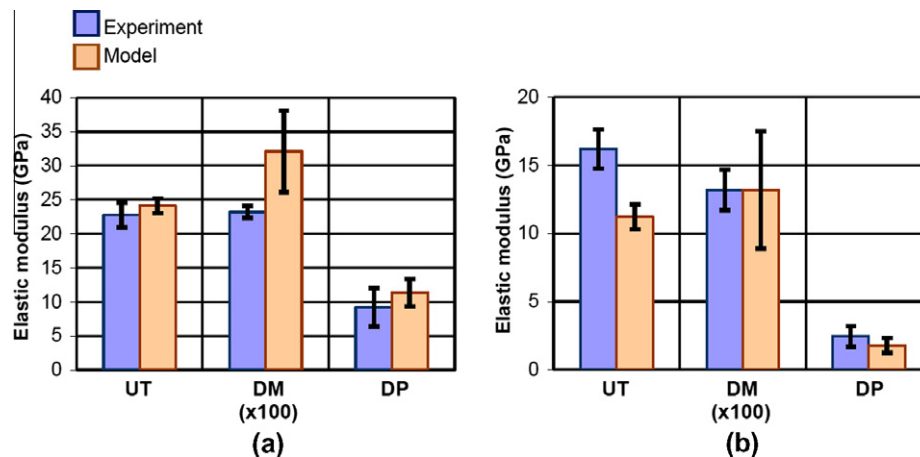


**Fig. 8.** Comparison of the experimental and modeling results for (a) longitudinal, and (b) transverse elastic moduli of untreated (UT), demineralized (DM) (magnified 100× for clarity) and deproteinized (DP) cortical bone. The capped lines show the standard deviation for experimental data and the range for modeling results.

oriented perpendicular to the main Haversian system (see Fig. 4), was neglected. Including some voids in the transverse direction (Volkmann's canals) would decrease the computed elastic moduli of DM bone, along with considering the off-axis alignment of the Haversian canals. Another reason for the difference of experimental and modeling results for DM bone is a possible degradation of collagen structure during the demineralization process due to enzymatic autolysis [25].

In the case of DP bone, the results of modeling and experiments could be closer if more information about the type and magnitude of forces that hold the hydroxyapatite crystals together were available. In the present model, it was assumed that, after removing the protein phase, hydroxyapatite crystals were perfectly bonded to each other. Based on SEM images shown in Fig. 9, the hydroxyapatite crystals in DP bone form an aligned nanocrystalline network, coinciding with the collagen alignment. These nanocrystals are most likely held together by weak electrostatic forces and/or through mechanical interlocking, as demonstrated by the low fracture strength shown in Fig. 6c. Incorporating such geometry that could allow some slip in the model could give rise to a better match
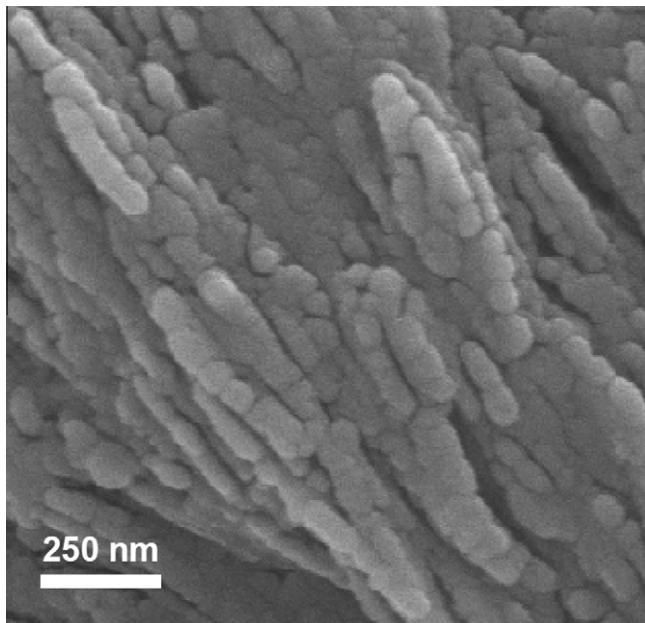
**Fig. 9.** SEM micrograph of DP bone (100% minerals) showing that minerals align in a preferred orientation. This alignment coincides with the alignment of the collagen fibers.
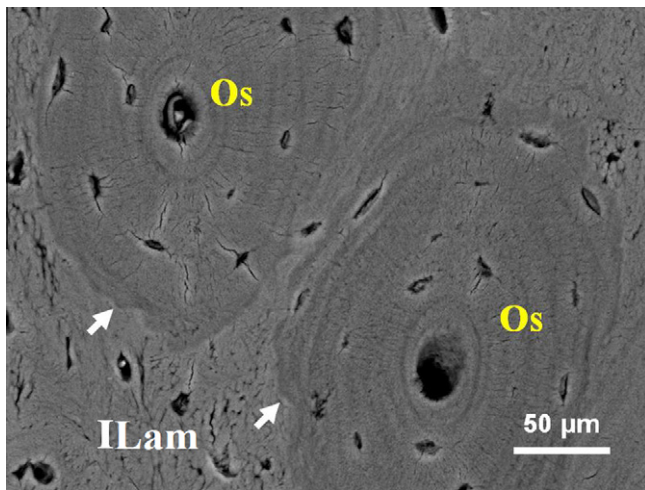


**Fig. 10.** Backscattered electron image showing the cross-sectional microstructure of cortical bovine femur bone: osteons (Os); interstitial lamellae (ILam); arrows point to the cement lines.

between the actual and the modeled structure and, consequently, elastic properties of DP bone.

Another limitation of the present model is neglecting the presence of cement lines around the outer boundaries of osteons. These thin (<5 μm) lines deflect crack propagation in bone loaded in the transverse direction, which enhances the fracture toughness of the bone in this direction [81]. A backscattered SEM image of cortical bone is shown in Fig. 10, where the presence of cement lines is clearly observed around the osteons. There is no consensus in the literature on the DOM of cement lines. Some researchers found that cement lines are less mineralized than the surrounding tissues [82], while others described cement lines as highly mineralized tissues [83]. In either case, since the volume fraction of thin cement lines is very small compared with the volume fractions of osteons and interstitial lamella, their presence does not significantly affect the computed elastic moduli of all three bone groups. However,

while studying the strength and fracture of cortical bone, the important role of cement lines should not be ruled out.

In summary, the present multi-scale model assumed that cortical bone is an interpenetrating composite of continuous phases of collagen and hydroxyapatite. The model also accounted for the presence of NCP, water and porosity. The experimental inputs were the volume fractions of porosities at different levels obtained from μ-CT scans and the volume fractions of osteonal and interstitial bone obtained from OM. Additionally, the morphology of the collagen fibrils, hydroxyapatite and porosity was incorporated using the Eshelby tensor. Given the simplifying assumptions used in the analysis, the model showed very good agreement with experimental values. To the authors' knowledge, this is the first multi-scale model that incorporates experimental observations of bone as an interpenetrating composite material. Also, the study of DM and DP bone, which provided valuable insights into the bone structure and its mechanical properties, allowed fine tuning of the theoretical model.

## 5. Conclusions

A new theoretical model was developed that accurately predicts the experimentally measured elastic modulus of cortical bovine femur bone. This model assumes that cortical bone has a hierarchical structure, is an interpenetrating composite of biopolymers and hydroxyapatite minerals, and consists of porosity at different hierarchical levels. A bottom-up approach was employed, incorporating outcomes of the previous hierarchical level as the inputs for the next one. This model was further verified by the close agreement found between the model and experimental results taken on DP and DM bone.

The major findings of this work are as follows.

1. This is the first multi-scale model incorporating experimental observations of bone as an interpenetrating composite combined with interdispersed porosity at different hierarchical levels. These results show the complexity of the bone structure, which is still not well understood, and the open challenges in modeling it.
2. The compressive elastic moduli of UT and treated bones show anisotropy in the elastic modulus between the longitudinal (higher) and transverse (lower) directions. This demonstrates that both the protein and mineral architectures have preferential structures in the longitudinal direction.
3. Three-dimensional imaging by μ-CT clearly reveals and quantifies the hierarchical structure of the porosity from lacuna spaces to vascular channels and to resorption cavities. The lacunae spaces are ellipsoids that have the major axis parallel to the long axis of the bone. The μ-CT images illustrate a complex network of canals, including Haversian and Volkmann's canals, perforating the bone structure.
4. The multi-scale model using experimental values of porosity and volume fractions of constituents demonstrates that the elastic moduli of the UT, DM and DP bones are in very good agreement with the experimentally measured values.

## Conflict of interest statement

None of the authors have any conflicts of interest to report with respect to the material contained in this manuscript.

## Acknowledgements

## Appendix A

Given the Young's modulus $E_r$ and Poisson's ratio $v_r$ of a phase $r$ with an isotropic elastic behavior, its elastic stiffness tensor $\mathbf{C}_r$ is represented as

$$\mathbf{C}_r = \frac{E_r}{(1+v_r)(1-2v_r)} \begin{pmatrix} 1-v_r & v_r & v_r & 0 & 0 & 0 \\ v_r & 1-v_r & v_r & 0 & 0 & 0 \\ v_r & v_r & 1-v_r & 0 & 0 & 0 \\ 0 & 0 & 0 & 1-2v_r & 0 & 0 \\ 0 & 0 & 0 & 0 & 1-2v_r & 0 \\ 0 & 0 & 0 & 0 & 0 & 1-2v_r \end{pmatrix} . \tag{A.1}$$

Young's moduli and Poisson's ratios of different phases (collagen, hydroxyapatite, and water and NCP), which are given in Table 1, were substituted in Eq. (A.1) to obtain their corresponding elastic stiffness tensors.

## Appendix B. Figures with essential colour discrimination

Certain figure in this article, particularly Figures 1–8 and 10, is difficult to interpret in black and white. The full colour images can be found in the on-line version, at doi:10.1016/j.actbio.2011.11.010.

## References

[1] Olszta MJ, Cheng XG, Jee SS, Kumar R, Kim YY, Kaufman MJ, et al. Bone structure and formation: a new perspective. Mater Sci Eng R 2007;58:77–116.
[2] Fratzl P, Weinkamer R. Nature's hierarchical materials. Prog Mater Sci 2007;52:1263–334.
[3] Rho JY, Kuhn-Spearing L, Zioupos P. Mechanical properties and the hierarchical structure of bone. Med Eng Phys 1998;20:92–102.
[4] Weiner S, Wagner HD. The material bone: structure mechanical function relations. Annu Rev Mater Sci 1998;28:271–98.
[5] Orgel JPRO, Miller A, Irving TC, Fischetti RF, Hammersley AP, Wess TJ. The in situ supermolecular structure of type I collagen. Structure 2001;9:1061–9.
[6] Parry DAD, Craig AS. Growth and development of collagen fibrils in connective tissue. In: Ruggeri A, Motta PM, editors. Ultrastructure of the connective tissue matrix. Boston: Martinus Nijhoff; 1984. p. 34–63.
[7] Miller A. Collagen: the organic matrix of bone. Philos Trans R Soc Lond B Biol Sci 1984;304:455–77.
[8] Schmitt FO, Hall CE, Jakus MA. Electron microscope investigations of the structure of collagen. J Cell Comp Physiol 1942;20:11–33.
[9] Orgel JPRO, Irving TC, Miller A, Wess TJ. Microfibrillar structure of type I collagen in situ. Proc Natl Acad Sci USA 2006;103:9001–5.
[10] Currey JD. Bones: structure and mechanics. Princeton: Princeton University Press; 2002.
[11] Jackson SA, Cartwright AG, Lewis D. Morphology of bone–mineral crystals. Calcif Tissue Res 1978;25:217–22.
[12] Rubin MA, Jasiuk I, Taylor J, Rubin J, Ganey T, Apkarian RP. TEM analysis of the nanostructure of normal and osteoporotic human trabecular bone. Bone 2003;33:270–82.
[13] Weiner S, Price PA. Disaggregation of bone into crystals. Calcif Tissue Int 1986;39:365–75.
[14] Ziv V, Weiner S. Bone crystal sizes – a comparison of transmission electron microscopic and X-ray diffraction line width broadening techniques. Connect Tissue Res 1994;30:165–75.
[15] Hang F, Barber AH. Nano-mechanical properties of individual mineralized collagen fibrils from bone tissue. J R Soc Interface 2011;8:500–5.
[16] Landis WJ, Hodgens KJ, Arena J, Song MJ, McEwen BF. Structural relations between collagen and mineral in bone as determined by high voltage electron microscopic tomography. Microsc Res Tech 1996;33:192–202.
[17] Landis WJ, Song MJ, Leith A, McEwen L, McEwen BF. Mineral and organic matrix interaction in normally calcifying tendon visualized in 3 dimensions by high-voltage electron-microscopic tomography and graphic image reconstruction. J Struct Biol 1993;110:39–54.
[18] Bonar LC, Lees S, Mook HA. Neutron-diffraction studies of collagen in fully mineralized bone. J Mol Biol 1985;181:265–70.
[19] Katz EP, Li S. Structure and function of bone collagen fibrils. J Mol Biol 1973;80:1–15.
[20] Nikolov S, Raabe D. Hierarchical modeling of the elastic properties of bone at submicron scales: the role of extrafibrillar mineralization. Biophys J 2008;94:4220–32.
[21] Pidaparti RMV, Chandran A, Takano Y, Turner CH. Bone mineral lies mainly outside collagen fibrils: predictions of a composite model for osteonal bone. J Biomech 1996;29:909–16.
[22] Sasaki N, Tagami A, Goto T, Taniguchi M, Nakata M, Hikichi K. Atomic force microscopic studies on the structure of bovine femoral cortical bone at the collagen fibril–mineral level. J Mater Sci Mater Med 2002;13:333–7.
[23] Castro-Ceseña AB, Novitskaya EE, Chen P-Y, Hirata GA, McKittrick J. Kinetic studies of bone demineralization at different HCl concentrations and temperatures. Mater Sci Eng C 2011;31:523–30.
[24] Chen P-Y, Toroian D, Price PA, McKittrick J. Minerals form a continuum phase in mature cancellous bone. Calcif Tissue Int 2011;88:351–61.
[25] Novitskaya E, Chen PY, Lee S, Castro-Ceseña A, Hirata G, Lubarda VA, et al. Anisotropy in the compressive mechanical properties of bovine cortical bone and the mineral and protein constituents. Acta Biomater 2011;7:3170–7.
[26] Remaggi F, Cane V, Palumbo C, Ferretti M. Histomorphometric study on the osteocyte lacuno-canalicular network in animals of different species. I. Woven-fibered and parallel fibered bones. Ital J Anat Embryol 1998;103:145–55.
[27] McCreadie BR, Hollister SJ, Schaffler MB, Goldstein SA. Osteocyte lacuna size and shape in women with and without osteoporotic fracture. J Bimech 2004;37:563–72.
[28] Reilly GS, Knapp HF, Stemmer A, Niederer P, Knothe Tate ML. Investigation of the morphology of the lacunacanalicular system of cortical bone using atomic force microscopy. Ann Biomed Eng 2001;29:1074–81.
[29] Giraud-Guille MM. Twisted plywood architecture of collagen fibrils in human compact bone osteons. Calcif Tissue Int 1988;42:167–80.
[30] Giraud-Guille MM. Plywood structures in nature. Curr Opin Solid State Mater Sci 1998;3:221–7.
[31] Chen P-Y, McKittrick J. Compressive mechanical properties of demineralized and deproteinized cancellous bone. J Mech Behav Biomed Mater 2011;4:961–73.
[32] Currey JD. Relationship between stiffness and mineral content of bone. J Biomech 1969;2:477–80.
[33] Katz JL. Hard tissue as a composite material. I. Bounds on elastic behavior. J Biomech 1971;4:455–73.
[34] Hellmich C, Barthelemy JF, Dormieux L. Mineral–collagen interactions in elasticity of bone ultrastructure – a continuum micromechanics approach. Eur J Mech A 2004;23:783–810.
[35] Hellmich C, Ulm FJ. Are mineralized tissues open crystal foams reinforced by crosslinked collagen? – some energy arguments. J Biomech 2002;35:1199–212.
[36] Fritsch A, Hellmich C. 'Universal' microstructural patterns in cortical and trabecular, extracellular and extravascular bone materials: micromechanics-based prediction of anisotropic elasticity. J Theor Biol 2007;244:597–620.
[37] Ji BH, Gao HJ. Elastic properties of nanocomposite structure of bone. Compos Sci Technol 2006;66:1212–8.
[38] Kotha SP, Guzelsu N. The effects of interphase and bonding on the elastic modulus of bone: changes with age-related osteoporosis. Med Eng Phys 2000;22:575–85.
[39] Siegmund T, Allen MR, Burr DB. Failure of mineralized collagen fibrils: modeling the role of collagen cross-linking. J Biomech 2008;41:1427–35.
[40] Yuan F, Stock SR, Haeffner DR, Almer JD, Dunand DC, Brinson LC. A new model to simulate the elastic properties of mineralized collagen fibril. Biomech Model Mechanobiol 2011;10:147–60.
[41] Jasiuk I, Ostoja-Starzewski M. Modeling of bone at a single lamella level. Biomech Model Mechanobiol 2004;3:67–74.
[42] Yoon YJ, Cowin SC. The estimated elastic constants for a single bone osteonal lamella. Biomech Model Mechanobiol 2008;7:1–11.
[43] Dong XN, Guo XE. Prediction of cortical bone elastic constants by a two-level micromechanical model using a generalized self-consistent method. J Biomech Eng 2006;128:309–16.
[44] Keller TS, Liebscher MAK. Tensile and compression testing of bone. In: An YH, Draughn RA, editors. Mechanical testing of bone and the bone–implant interface. Boca Raton: CRC Press LLC; 2000. p. 178–81.
[45] An YH, Bensen CV. General considerations of mechanical testing. In: An YH, Draughn RA, editors. Mechanical testing of bone and the bone–implant interface. New York: CRC Press; 1999. p. 120–2.
[46] Toroian D, Lim JE, Price PA. The size exclusion characteristics of type I collagen – implications for the role of noncollagenous bone constituents in mineralization. J Biol Chem 2007;282:22437–47.
[47] Basillais A, Bensamoun B, Chappard C, Brunet-Imbault B, Lemineur G, Ilharreborde B, et al. Three-dimensional characterization of cortical bone microstructure by microcomputed tomography: validation with ultrasonic and microscopic measurements. J Orthop Sci 2007;12:141–8.
[48] Hamed E, Lee Y, Jasiuk I. Multiscale modeling of elastic properties of cortical bone. Acta Mech 2010;213:131–54.
[49] Benveniste Y. A new approach to the application of Mori–Tanaka theory in composite materials. Mech Mater 1987;6:147–57.
[50] Mori T, Tanaka K. Average stress in matrix and average elastic energy of materials with misfitting inclusions. Acta Metall 1973;21:571–4.

[51] Eshelby JD. The elastic field outside an ellipsoidal inclusion. Proc R Soc Lond A 1959;252:561–9.

[52] Budiansky B. On elastic moduli of some heterogeneous materials. J Mech Phys Solids 1965;13:223–7.

[53] Hill R. Elastic properties of reinforced solids – some theoretical principles. J Mech Phys Solids 1963;11:357–72.

[54] Minary-Jolandan M, Yu MF. Nanoscale characterization of isolated individual type I collagen fibrils: polarization and piezoelectricity. Nanotechnology 2009;20.

[55] Robinson R. An electron microscopic study of the crystalline inorganic component of bone and its relationship to the organic matrix. J Bone Joint Surg 1952;344:389–435.

[56] Gavazzi AC, Lagoudas DC. On the numerical evaluation of Eshelby's tensor and its application to elastoplastic fibrous composites. Comput Mech 1990;7:13–9.

[57] Prostak KS, Lees S. Visualization of crystal–matrix structure. In situ demineralization of mineralized turkey leg tendon and bone. Calcif Tissue Int 1996;59:474–9.

[58] Sasaki N, Sudoh Y. X-ray pole figure analysis of apatite crystals and collagen molecules in bone. Calcif Tissue Int 1997;60:361–7.

[59] Benezra Rosen V, Hobbs LW, Spector M. The ultrastructure of anorganic bovine bone and selected synthetic hyroxyapatites used as bone graft substitute materials. Biomater 2002;23:921–8.

[60] Fratzl P, Schreiber S, Boyde A. Characterization of bone mineral crystals in horse radius by small-angle X-ray scattering. Calcif Tissue Int 1996;58:341–6.

[61] Lees S, Prostak KS, Ingle VK, Kjoller K. The loci of mineral in turkey leg tendon as seen by atomic-force microscope and electron microscopy. Calcif Tissue Int 1994;55:180–9.

[62] Fritsch A, Hellmich C, Dormieux L. Ductile sliding between mineral crystals followed by rupture of collagen crosslinks: experimentally supported micromechanical explanation of bone strength. J Theor Biol 2009;260:230–52.

[63] Fritsch A, Dormieux L, Hellmich C. Porous polycrystals built up by uniformly and axisymmetrically oriented needles: homogenization of elastic properties. C R Mecanique 2006;334:151–7.

[64] Hellmich C, Ulm FJ. Micromechanical model for ultrastructural stiffness of mineralized tissues. J Eng Mech 2002;128:898–908.

[65] Cheng L, Wang L, Karlsson AM. Image analyses of two crustacean exoskeletons and implications of the exoskeletal microstructure on the mechanical behavior. J Mater Res 2008;23:2854–72.

[66] Sun CT, Li S. Three-dimensional effective elastic constants for thick laminates. J Compos Mater 1988;22:629–39.

[67] Burr DB, Schaffler MB, Frederickson RG. Composition of the cement line and its possible mechanical role as a local interface in human compact bone. J Biomech 1988;21:939–45.

[68] Guo XE, Liang LC, Goldstein SA. Micromechanics of osteonal cortical bone fracture. J Biomech Eng 1998;120:112–7.

[69] Christensen RM, Lo KH. Solutions for effective shear properties in three phases sphere and cylinder models. J Mech Phys Solids 1979;27:315–30.

[70] Cowin SC. Bone mechanics handbook. Boca Raton: CRC Press; 2001.

[71] Taya M, Chou TW. On two kinds of ellipsoidal inhomogeneities in an infinite elastic body: an application to a hybrid composite. Int J Solids Struct 1981;17:553–63.

[72] Gibson LJ, Ashby MF. Cellular solids – structure and properties. 2nd ed. Cambridge: Cambridge University Press; 1997.

[73] Ascenzi A. The micromechanics versus the macromechanics of cortical bone – a comprehensive presentation. J Biomech Eng 1988;110:357–63.

[74] Riggs CM, Vaughan LC, Evans GP, Lanyon LE, Boyde A. Mechanical implications of collagen fibre orientation in cortical bone of the equine radius. Anat Embryol (Berl) 1993;187:239–48.

[75] Currey JD. The effect of porosity and mineral content on the Young's modulus of elasticity of compact bone. J Biomech 1988;21:131–9.

[76] Schaffler MB, Burr DB. Stiffness of compact bone: effects of porosity and density. J Biomech 1988;21:13–6.

[77] Gibson LJ, Ashby MF. The mechanics of three-dimensional cellular materials. Proc R Soc Lond A 1982;382:25–42.

[78] Robling AG, Stout SD. Morphology of the drifting osteon. Cells Tissues Organs 1999;164:192–204.

[79] Jager I, Fratzl P. Mineralized collagen fibrils: a mechanical model with a staggered arrangement of mineral particles. Biophys J 2000;79:1737–46.

[80] Gupta HS, Stachewicz U, Wagermaier W, Roschger P, Wagner HD, Fratzl P. Mechanical modulation at the lamellar level in osteonal bone. J Mater Res 2006;21:1913–21.

[81] Koester KJ, Ager JW, Ritchie RO. The true toughness of human cortical bone measured with realistically short cracks. Nat Mater 2008;7:672–7.

[82] Schaffler MB, Burr DB, Fredrickson RG. Morphology of the cement line in human bone. Anat Rec 1987;217:223–8.

[83] Skedros JG, Holmes JI, Vajda EG, Bloebaum RD. Cement lines of secondary osteons in human bone are not mineral-deficient: new data in a historical perspective. Anat Rec A 2006;286:781–803.

[84] Hall RH. Variations with pH of the tensile properties of collagen fibres. J Soc Leather Trades Chem 1951;35:195–210.

[85] Gilmore RS, Katz JL. Elastic properties of apatites. J Mater Sci 1982;17:1131–41.

[86] Katz JL, Ukraincik K. On the anisotropic elastic properties of hydroxyapatite. J Biomech 1971;4:221–7.

[87] Snyders R, Music D, Sigumonrong D, Schelnberger B, Jensen J, Schneider JM. Experimental and ab initio study of the mechanical properties of hydroxyapatite. Appl Phys Lett 2007;90.